Supplementary figures

Supplementary Figure 1

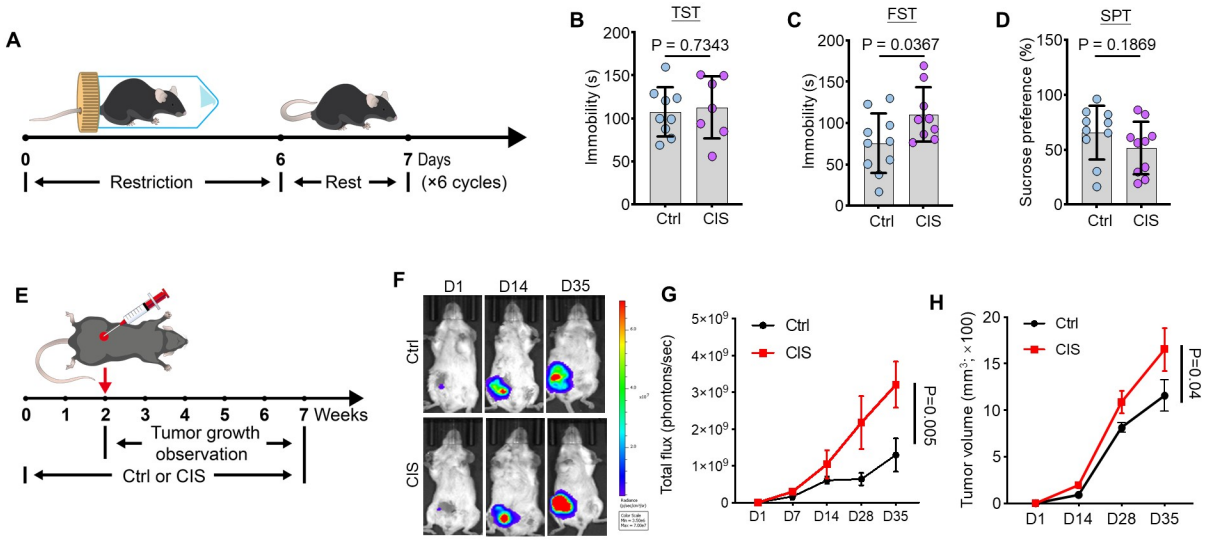

Supplementary Figure 1. **Behavioral and Tumor Growth Changes in Chronic Immobilization Stress (CIS)-Exposed Mice**. (A) A schematic illustrates the experimental paradigm employed to induce chronic immobilization stress (CIS) in mice. Animals were subjected to daily immobilization within 50 ml Eppendorf centrifuge tubes for 2 hours per day, 6 days per week, over a continuous period of 6 weeks to establish the CIS-exposed mouse model. (B) Tail Suspension Test (TST). Duration of immobility in control (Ctrl) and CIS-exposed mice. (C) Forced Swimming Test (FST). Duration of immobility in Ctrl and CIS-exposed mice. (D) Sucrose Preference Test (SPT). Sugar water preference rate in Ctrl and CIS-exposed mice. (E) Experimental Design for Tumor Growth Observation in CIS-Exposed Mice. Breast cancer cells were implanted in CIS-exposed mice after 2 weeks of stress exposure, followed by a 5-week observation period for tumor growth. (F) Representative In Vivo Imaging System (IVIS) Images. Luciferin signal in Ctrl and CIS mice on days 1, 14, and 35 following subcutaneous implantation of luciferase-expressing 4T1 cells adjacent to the mammary fat pad. n=10 mice per group. (G) Quantification of the total luciferin signal flux within the implantation area. (H) An orthotopic tumor growth curve showing the tumor volume changes in Ctrl and CIS-exposed mice over the observation period. n=10 mice per group. All data are presented as mean ± SD. Analysis: unpaired Student's t test.

Supplementary Figure 2

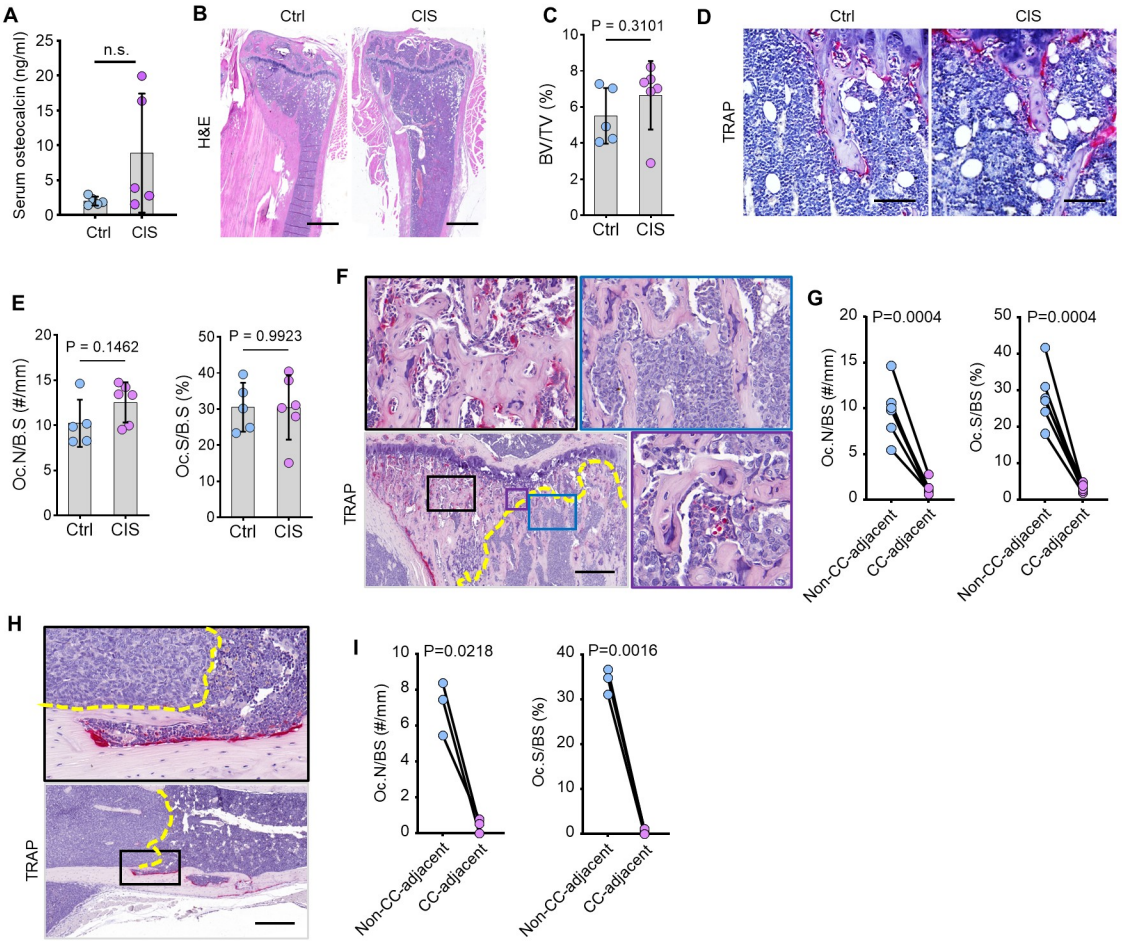

Supplementary Figure 2. **Histological analysis of trabecular bone volume and osteoclastic bone resorption in CIS-exposed mice**. (A) ELISA test on osteocalcin levels in serum from Ctrl and CIS-exposed mice. n=5 mice per group. (B) Representative images of HE-stained paraffin sections showing the coronal plane of tibiae from Ctrl and CIS-exposed mice. Bar=500 µm. (C) Quantification of trabecular bone volume of tibiae from Ctrl and CIS-exposed mice. n=5 Ctrl and 6 CIS-exposed mice. (D) Representative images of TRAP-stained paraffin sections showing osteoclasts (red) on trabecular bone surfaces. Bar=50 µm. (E) Quantification of osteoclast number and surface on trabecular bone surfaces. n=5 Ctrl and 6 CIS-exposed mice. (F) Representative TRAP-staining images showing the difference of osteoclasts in metastatic tumor area (blue rectangle) and non-tumor area (black rectangle), and osteoclast apoptosis at the edge of these two area (purple rectangle) in metaphyseal trabecular bone region. Bar=250 µm. (G) Quantification of osteoclast number and surface on trabecular bone surfaces in non-cancer cell (CC)-adjacent area and CC-adjacent area. n=6 mice per group. (H) Representative TRAP-staining images showing the difference of osteoclasts in metastatic tumor area and non-tumor area in diaphyseal cortical bone region. Bar=250 µm. (I) Quantification of osteoclast number and surface on cortical bone surfaces in non-CC-adjacent area and CC-adjacent area. n=3 mice per group. All data are presented as mean ± SD. Analysis: unpaired Student's t test.

Supplementary Figure 3

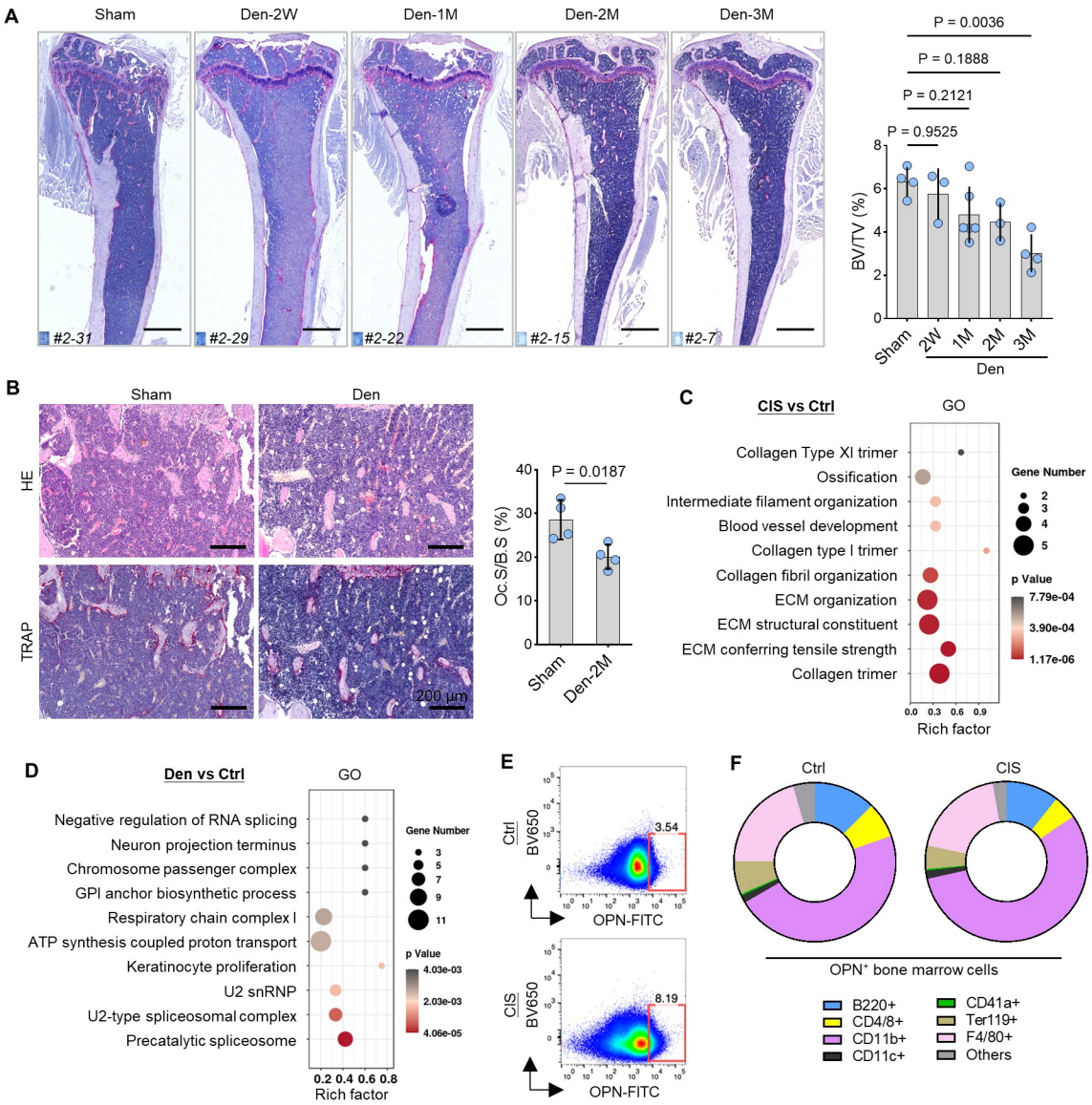

Supplementary Figure 3. **Histological analysis of trabecular bone volume and osteoclastic bone resorption in denervation mice**. (A) Representative images of TRAP-stained paraffin sections showing coronal plane of tibiae from sham and denervation mice at different time points post denervation surgery. Quantification of trabecular bone volume in metaphyseal region. n=3 to 5 mice in various groups. Bar=500 μm. (B) Representative HE- and TRAP-staining images of tibial coronal paraffin sections from sham and denervation mice 2 months post surgery. Quantification of osteoclast surfaces on trabecular bone surfaces. n=4 mice per group. Bar=200 μm. (C) The Top10 signaling pathways basing on GO analysis of significantly changed proteins in BM cells of CIS mice versus Ctrl mice using mass spectrum. (D) The Top10 signaling pathways basing on GO analysis of significantly changed proteins in BM cells of denervated mice versus sham mice. (E) Flow gates for counting osteopontin (OPN)-positive cells in total bone marrow cells from control (Ctrl) and CIS-exposed mice. (F) A pie graph showing the composition of OPN-positive bone marrow cells, including B cells (B220+), T lymphocytes (CD4+ and CD8+), myeloid cells (CD11b+), dendritic cells (CD11c+), megakaryocytes (CD41a+), erythrocytes (Ter119+), macrophages (F4/80+) and others, from Ctrl and CIS-exposed mice. All data are presented as mean ± SD. Analysis: One-way ANOVA test with Tukey post analysis in (A); unpaired Student's t test in (B).

Supplementary Figure 4

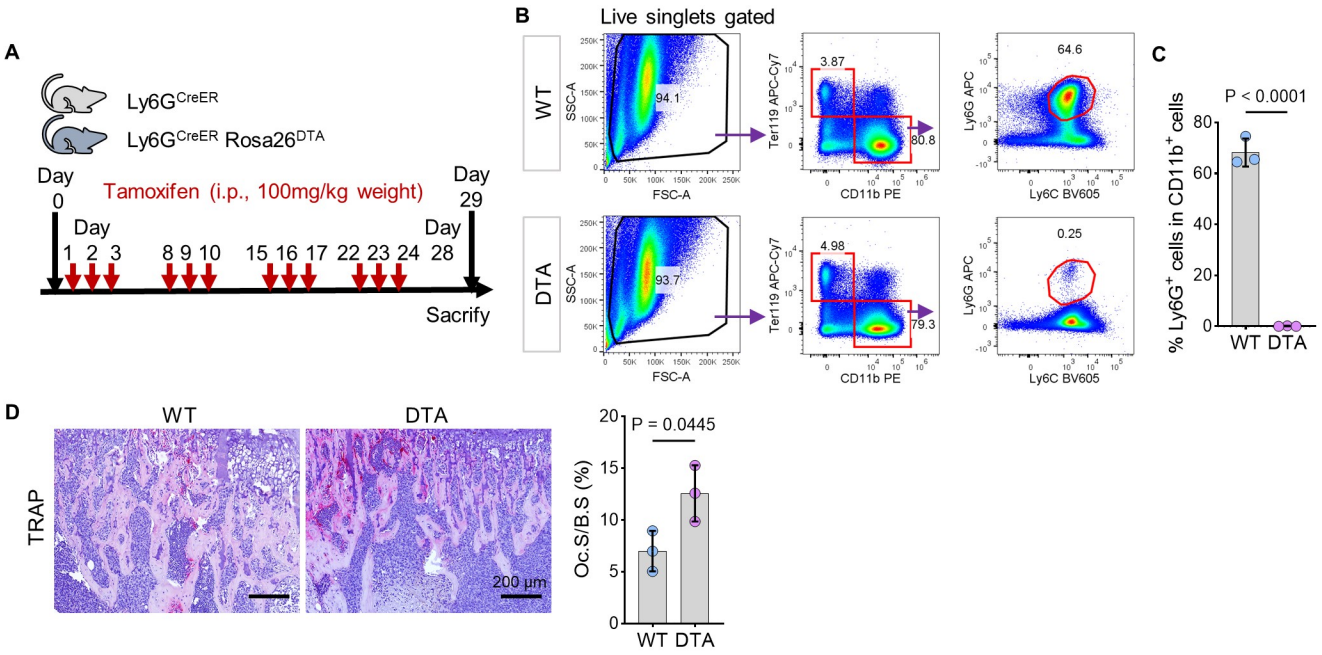

Supplementary Figure 4. **The efficiency of neutrophil clearance and osteoclast activity in Ly6G^{CreER}Rosa26^{DTA} (Ly6G-DTA) mice**. (A) A schematic illustrates the experimental paradigm employed to induce specific neutrophil clearance in Ly6G-DTA mice following I.P. injection of tamoxifen (100 mg/Kg body weight). (B) Representative flow graphs of gating CD11b+Ly6G+ cells from live bone marrow singlets from Rosa26^{DTA} (WT) and Ly6G^{CreER}Rosa26^{DTA} (Ly6G-DTA) mice after tamoxifen administration. (C) Comparison of the frequencies of Ly6G^{+} neutrophils in CD11b^{+} myeloid lineage cells in bone marrow from WT and Ly6G-DTA mice. (D) Representative TRAP-staining images of tibial coronal paraffin sections from WT and Ly6G-DTA mice. Quantification of osteoclast surfaces on trabecular bone surfaces. Bar=200 μm. n=3 mice per group. All data are presented as mean ± SD. Analysis: unpaired Student's *t* test.

Supplementary Figure 5

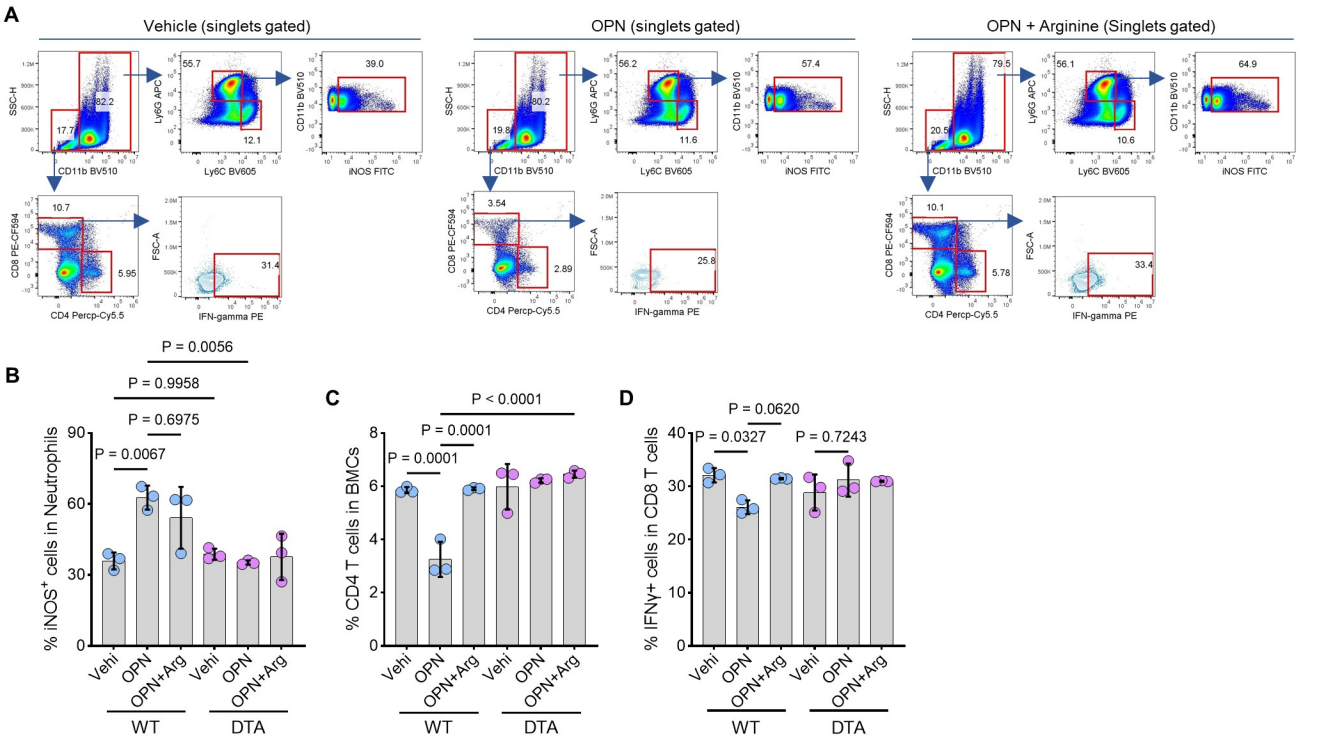

Supplementary Figure 5. **Neutrophil depletion and arginine administration effectively prevents effects of OPN on neutrophils and T cells**. (A) Representative flow graphs shows the gates for iNOS+ neutrophils and IFNγ+ CD8 lymphocytes in bone marrow cells (BMCs) treated with vehicle or OPN plus arginine. (B) Frequencies of iNOS-positive cells in neutrophils (CD11b+Ly6G+) in BMCs from WT and Ly6G-DTA mice, treated with vehicle or OPN plus arginine. (C) Frequencies of CD4 T lymphocytes in total BMCs, and (D) frequencies of IFNγ+ cells in CD8 T lymphocytes in BMCs from WT and Ly6G-DTA mice, treated with vehicle or OPN plus arginine. All data are presented as mean ± SD. Analysis: One-way ANOVA test with Tukey post analysis.

Supplementary Figure 6

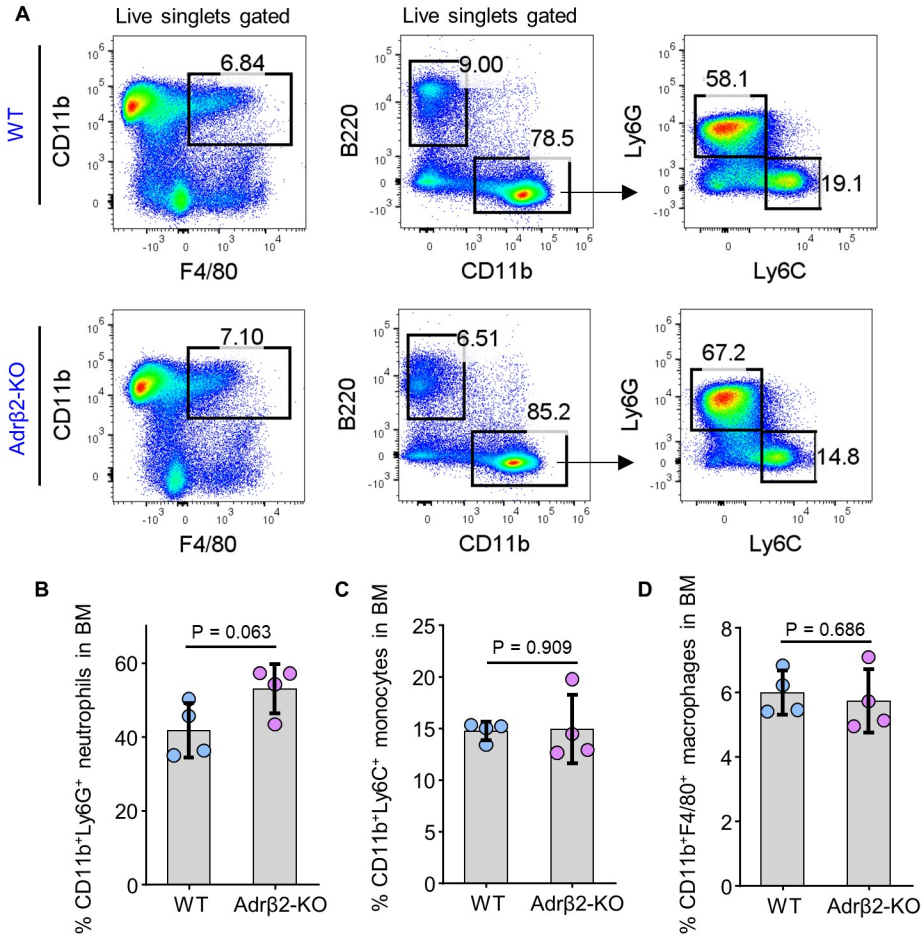

Supplementary Figure 6. **The changes of neutrophils, monocytes and macrophages in BMCs from Adrβ2-KO mice**. (A) Representative flow graphs of gating macrophages ($CD11b^+F4/80^+$), monocytes ($CD11b^+Ly6C^+$) and neutrophils ($CD11b^+Ly6G^+$) in total BMCs from Adrβ2 global knockout (Adrβ2-KO) and WT mice. (B-D) The frequencies of macrophages ($CD11b^+F4/80^+$), monocytes ($CD11b^+Ly6C^+$) and neutrophils ($CD11b^+Ly6G^+$) in total BMCs from Adrβ2-KO and WT mice. n=4 mice per group. All data are presented as mean ± SD. Analysis: unpaired Student's *t* test.

Supplementary Figure 7

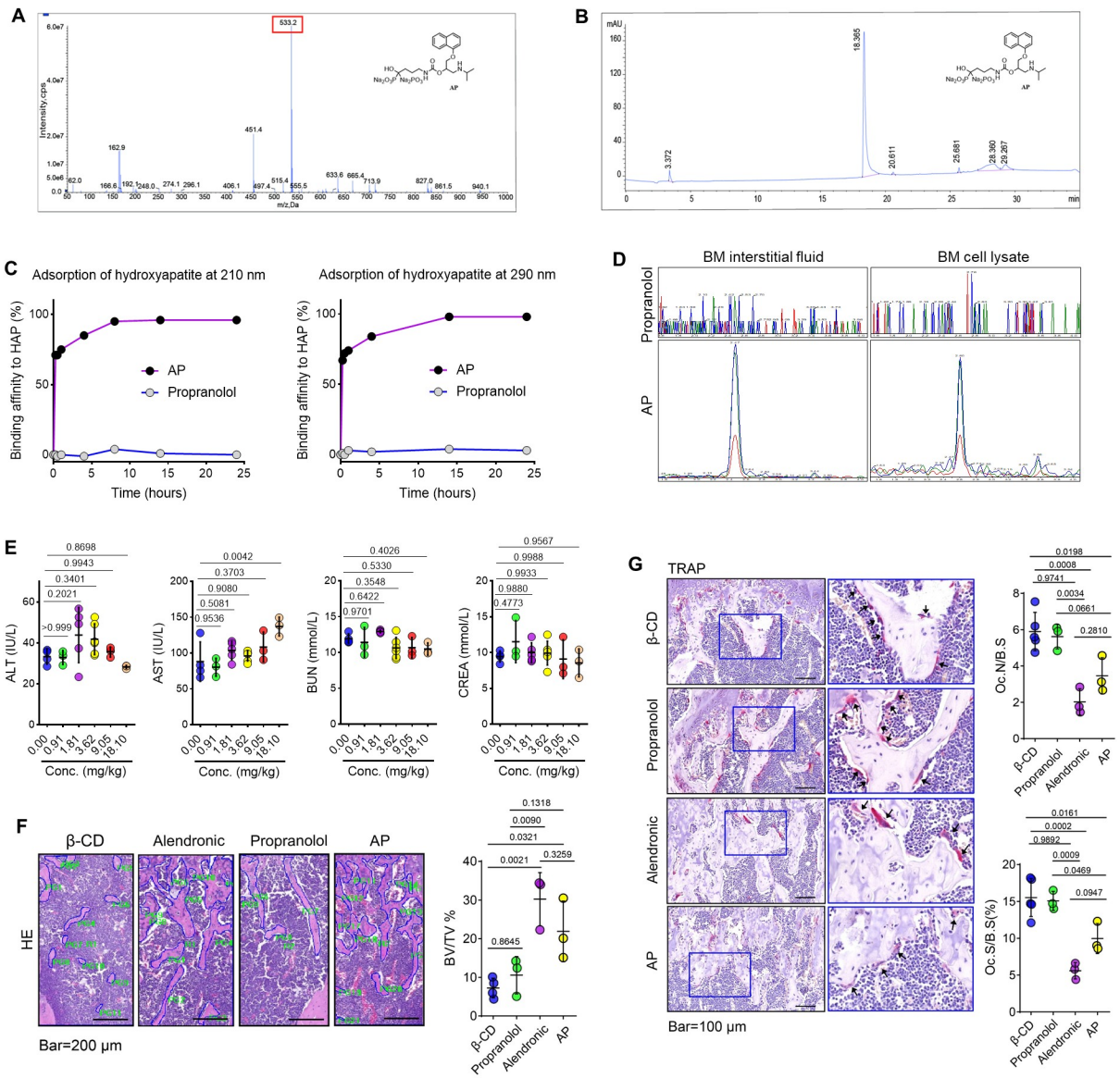

Supplementary Figure 7. **Evaluation of bone-targeting efficiency and effects on bone of alendronate-conjugated propranolol (AP)**. (A) Mapping of the compound Alendronate-propranolol (AP) using electrospray ionization mass spectrometry (ESI-MS). (B) HPLC chromatogram of AP. (C) Binding kinetics of propranolol hydrochloride and AP binding with hydroxyapatite (HAP) measured at 210 nm and 290 nm. (D) Measurement of propranolol levels in bone marrow cells and interstitial fluid from leg bones of lower limbs of propranolol- and AP-treated mice. (E) Parameters of liver and renal toxicity, including ALT, AST, BUN and CREA, in serum of mice treated with various doses of AP. (F) Representative images of HE-stained tibial paraffin sections show trabecular bones in metaphyseal regions of mice treated with β-CD (vehicle), alendronate, propranolol and AP. Quantification of trabecular bone volume in metaphyseal of these mice. Bar=200 μm. (G) Representative images of TRAP-stained tibial paraffin sections show osteoclasts (Red) on trabecular bone surfaces. Quantification of osteoclast number and surface on trabecular bone surfaces in metaphyseal regions. Bar=100 μm. All data are presented as mean ± SD. Analysis: One-way ANOVA test with Tukey post analysis.

Supplementary Figure 8

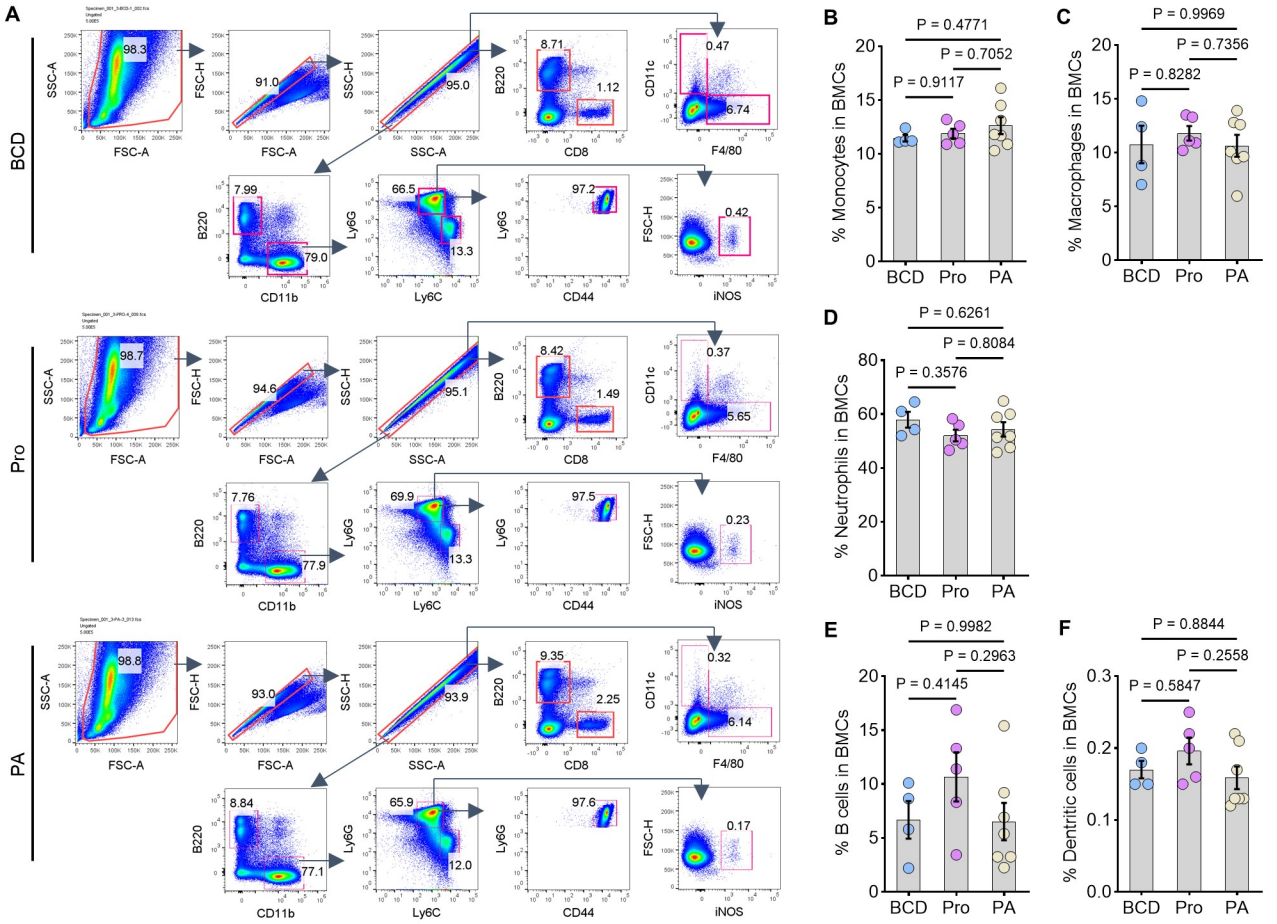

Supplementary Figure 8. **The changes of immune cells in BMCs of β-CD-, propranolol- and PA-treated mice**. (A) Representative flow graphs shows the gates for various immune cell populations in lymphoid and myeloid lineage cells. (B-F) Frequencies of monocytes ($CD11b^+Ly6C^+$; B) and macrophages ($F4/80^+$; C) neutrophils ($CD11b^+Ly6G^+$; D), B cells ($B220^+$; E), dendritic cells ($CD11c^+$; F) in total BMCs from β-CD-, propranolol- and PA-treated mice. n=4, 5 and 7 mice for β-CD-, propranolol- and PA-treated groups, respectively. All data are presented as mean ± SD. Analysis: One-way ANOVA test with Tukey post analysis.